THE VARIABILITY OF SEA LEVEL AND ITS IMPACT ON COASTAL FLOODING IN BAÍA DE TODOS SANTOS (13oS)

Guilherme C Lessa, Gabriel L Pugliese, Felipe M Santos, Pablo A dos Santos, Carlos E P Teixeira, Martinho Marta-Almeida

https://doi.org/10.1590/2675-2824074.250232

Submitted on: 2026-05-27
Posted on: 2026-05-27 (version 1)
(YYYY-MM-DD)

Ocean and Coastal Research

Original Article

http://dx.doi.org/10.1590/2675-2824074.250232

ISSN 2675-2824

Variability of sea-level and flooding in Salvador

THE VARIABILITY OF SEA LEVEL AND ITS IMPACT ON COASTAL FLOODING IN BAÍA DE TODOS SANTOS (13ºS)

Guilherme C. Lessa[1], Gabriel L. Pugliese [1,2], Felipe M. Santos[3] , Pablo A. dos Santos[2] , Carlos E.P. Teixeira[4], Martinho Marta-Almeida[5]

G.C.L.: https://orcid.org/0000-0002-0928-2441

G.L.P.: https://orcid.org/0009-0009-0503-9688

F.M.S.: https://orcid.org/0000-0002-2189-8855

P.A.S. https://orcid.org/0009-0006-7987-9354

C.E.P.T.: https://orcid.org/0000-0002-2868-8914

M.M.A.: https://orcid.org/0000-0001-8214-3096

1 Oceanography Department, Geoscience Institute, Federal University of Bahia, Brazil

2 Municipal Civil Protection of Salvador, Bahia, Brazil

3 SENAI-CIMATEC University, Salvador, Brazil

4 Universidade Federal do Ceará (UFC), Brazil

5 Centro Oceanografico de A Coruña, Instituto Español de Oceanografia (IEO-CSIC), A Coruña, Spain

* Corresponding author: gclessa@gmail.com

Abstract

This study uses 21 years (2004-2024) of water level measurements carried out by the IBGE's Brazilian Continuous Monitoring Network (RBMC), in association with the Global Level Observation Program (GLOOS), with the aim to quantify the temporal variability of the water level, identify long-term trends of the mean sea level and determine the present spatial extend of tidal inundation of the suburban areas of Salvador. Harmonic, statistical and spectral analyses, complemented by numerical modeling of the hydrodynamics, show that the sea level is rising at a rate of 2.15 mm/year and the inundation time is increasing. Important seasonal variability is observed, with higher mean sea levels occurring in May and April driven mainly by the wind shear, whose interannual variation also causes alternate interannual MSL trends. The data indicates an increase in the frequency and severity of extreme high sea level events, regularly associated with the transit of subtidal waves that have become higher and more frequent along the years. Numerical simulations showed that subtidal oscillations tend to be

amplified inside the estuary, likely increasing the severity of inundation events. A suburban area of 496,513 m^2 along the bay margin of Salvador, with poor infrastructure, is undergoing tidal inundation that has become more intense every 4 years.

Keywords: SUB-INERTIAL OSCILLATIONS, SEA-LEVEL RISE, NUMERICAL MODEL, MONITORING

Introduction

The sea level is a fundamental reference for human occupation along the coast. It not only limits the seaward expansion of human settlements but also establishes boundaries for different activities, such as navigation, farming and recreation, and sets an altitudinal reference for urban planning. The sea level is influenced by periodic and non-periodic oscillations over a large spectrum of frequencies, which for the purpose of coastal management varies from high frequency oscillations related to infragravity waves and wave set up (Dodet et al. 2019) to very low frequencies related to interannual climate variability, nodal tidal cycle and even secular changes. The interaction of these different oscillations causes considerable complexity in the sea level variability. Extreme high-water levels and coastal inundation occurs when the phase of various of these oscillations concur, elevating sea level beyond a historical reference elevation used by urban planners.

Subjacent to these interactions is the present global-mean sea-level rise (GMSLR), an anthropogenically-forced phenomenon initiated in the 19th century (Jevrejeva et al., 2009; Church and White, 2011) and associated with an increase in the ocean volume due to both steric expansion and melting of ice sheets. A linear trend of tide gauge data between 1900 and 2009 indicates the GMSLR increased at a rate of 1.7 mm/y, but that increases to 3.2 mm/y if satellite altimetry from 1993-2009 is analyzed (Church and White, 2011). More recently, Hamlington et al. (2024) suggested that a linear fit on long time series can be misleading because it diminishes the impact of acceleration in sea-level trends. The global mean acceleration measured by satellite altimetry since 1993 is 0.08 ± 0.06 mm/y2, and caused the sea-level rising rate to augment from 2.1 mm/y to 4.5 mm/y in 2023 (Hamlington et al. 2024).

GMSLR is a direct consequence of global warming, which also impacts coastal MSL as the energy stored in the atmosphere causes stronger winds (speed has increased by 0.074% annually since 1940 - Chen 2025), higher waves (+0.32 cm/yr between 1979 and 2018 – Zheng et al., 2022) and lower atmospheric pressures (the inverted barometer effect accounts for ~10–30% of sea level rise on the US East coast between 1950 and 2013 (Piecuch and Ponte, 2015)), whose effects add up to produce larger storm surges. Using a global storm surge numerical model forced with CMIP6 projections, Muis et al. (2023) suggested that half of the defined 35 coastal sectors worldwide will undergo some or significant increase in surge levels by 2050. Storms can impact the mean sea level of distant sites by generating coastal trapped waves (CTW) of subtidal frequency, that can travel thousands of kilometers away from the its center of origin. Freitas et al. (2021) has shown that CTW' generated by storms in Patagonia (65°S) can travel more than 4500 km, causing small subtidal sea level oscillations in Northeast Brazil (10°S).

But amongst the contributors for sea level oscillations, tides are by far the most important, with

a spectral power at least 3 orders of magnitude higher than oscillations excited by other phenomena (Harrison, 2002). The tidal wave is a compound of various harmonics with different amplitudes, frequencies and phases that cause sea level periodicities varying from hours to decades. Therefore, understanding the predictable site-specific tidal beating is important to evaluate the probability of inundation at a given time. Tidal oscillations can be, however, also impacted by the GMSLR, especially in coastal bays and estuaries. Pickering et al. (2012) investigated the impact of a 2m rise in the relative sea level in the North Sea and Irish Channel, and suggested that larger tidal ranges may occur in the majority of the area, with higher rates close to the coast where spring tidal range could locally increase by up to 35 cm. Inside estuaries opposing trends can occur depending on whether the topography of the marginal terrain will allow for the growth or reduction of intertidal areas. Oey et al. (2007) have shown that the inclusion of intertidal areas in a numerical model of Cook Inlet increased the tidal range by 20%, and tidal ranges in bays and estuaries around the U.K. have apparently increased in the Holocene accompanying an increase in water depth (Hinton, 1995; Shaw et al. 2010).

Nowadays, the Permanent Service for Mean Sea Level (PSMSL) archives data from about 2000 tide gauge stations worldwide, and the Global Sea Level Observing System at the University of Hawaii (GLOSS - UHSLC) provide access to about 600 operational tide gauge data. Data from 10 stations along the Brazilian coast were analyzed by Mesquita et al. (2013). The data extended from 1947 to 1967, not simultaneous for most of the stations, and indicated sea level rising rates between 3 mm/yr and 4 mm/yr. Recently, Efraime et al. (2025) analyzed more recent data from six stations maintained by the Brazilian Geographical Institute (IBGE) also part of the GLOSS network, all of them paired with a Global Navigation Satellite System (GNSS) station. All but 1 tide gauge station had more than 17 years of records, and two stations had records longer than 50 years. Their results indicate a relative sea level rise varying between 2.2 mm/y (Ilha Fiscal) and 4.3 mm/y (Cananéia). Their trend analysis on four tidal harmonic components showed increasing amplitude of M2 and S2 in the southern stations of Imbituba and Cananéia, at rates up to 0.55 mm/y. The authors also characterized seasonal and interannual variability, but due to lack of supplementary climatic time series no objective causal investigation was performed to explain the observed variability.

Here we will analyze the sea level signal at the IBGE station in Salvador, at the entrance of Baia de Todos os Santos (BTS - Figure 1) aiming to determine the variability of tidal ranges, the extreme mean high-water level, and the relative MSL rising rates. The BTS is the 3rd largest coastal bay in Brazil (Lessa et al., 2018) where, according the 2022 IBGE Census (IBGE, 2022), a population of 617,180 live along the bay margin, often with precarious infrastructure. Therefore, it is also an objective of the present study to quantify and evaluate the susceptibility of areas that are presently undergoing the effects of marine invasion along the suburban areas of the city of Salvador.

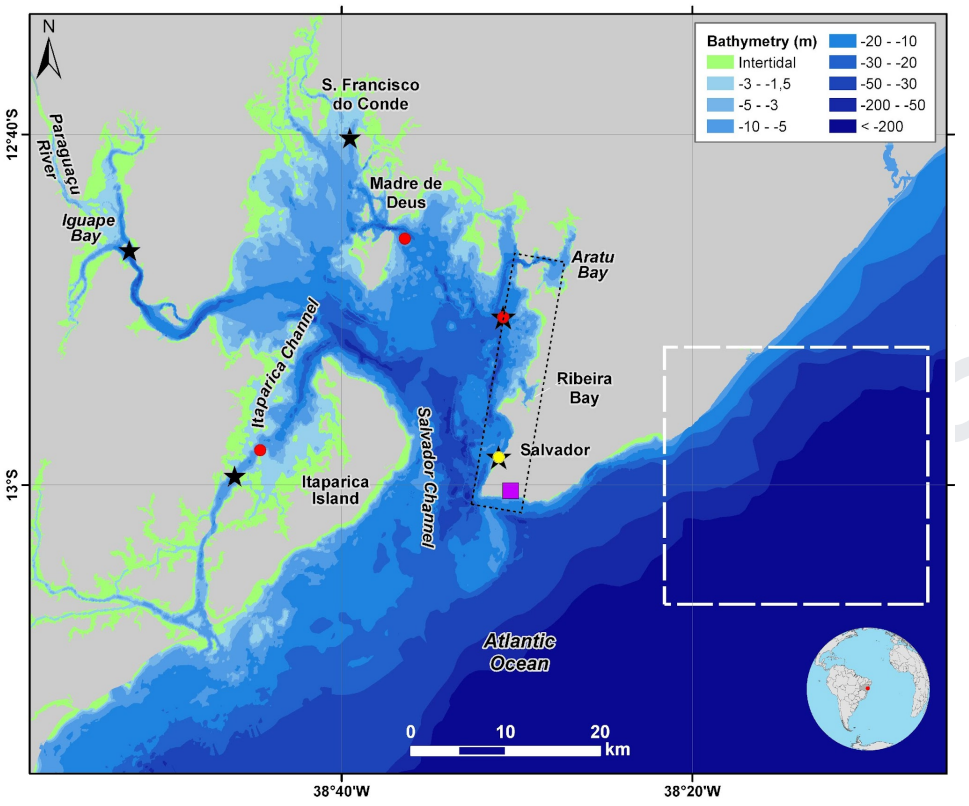

Figure 1 – Baía de Todos os Santos with location of the IBGE tide gauge (yellow dot), meteorological station (purple square), stations used to validate the simulated tides (red circles) and stations chosen to assess the propagation of the shelf waves (black stars). Dashed white square indicates the location of the Cross-Calibrated Multi-Platform (CCMP) grid element. Rectangle drawn in dotted black line delimits the section shown in Figure 13.

METHODS

Study Area

The BTS is a large (1,223 km^2) tectonic, well-mixed, positive estuary (Cirano and Lessa, 2007) centered at 12.83°S and situated behind the narrowest (10 to 15 km wide) stretch of the western South Atlantic continental shelf. The bay has maximum and average depths of 60 m and 9.6 m, respectively, with a main northern inlet (Salvador Channel, Figure 1) 10 km wide and 30 m deep, on average. The tides are semi-diurnal, with form numbers (F=K1+O1/M2+S2) varying from 0.11 on the shelf to 0.06 inside the bay, and explain 97.5% of sea-level variability. The tidal range on the shelf is amplified 1.5 times along the bay, with the main lunar semi-diurnal component (M2) growing from 0.67 m to 1.06 m 60 km upstream (Cirano and Lessa, 2007). The tides are asymmetric inside the bay, favoring a faster ebbing tide, and this asymmetry is increased landward.

The BTS catchment area is 61,110 km^2 (Lima and Lessa, 2002), with 90.5% of this area corresponding to the drainage of Paraguaçu River that reaches the bay in its western extreme

(Figure 1). The remaining of the catchment includes the rivers Jaguaripe (3.6%), Subaé (1.1%) and several small peripheral creeks (3.2%) (Lima and Lessa, 2002). The rainfall seasonality in the upper catchment is out-of-phase with that on the coast. Highest river discharges occur between November and March, the dry season on the coast. The Paraguaçu River accounts for 76% (69.5 m^3/s) of the total mean annual fluvial discharge that reaches the bay (Genz and Lessa 2015). This flux corresponds to 0.4% of the equinoctial spring-tidal prism of about 3.1×10^9 m^3 (Cirano and Lessa, 2007).

The wind blows from E-ENE in the summer and from ESE-SE in the winter, with a maximum mean speed of ~10m/s. E-ENE winds drive frequent coastal upwelling between September and March, which are longer lasting and more intense in front of the BTS (Santos et al., 2014; Thévenin et al., 2019). A 11-year wave time series obtained by a bottom-mounted ADCP on the continental shelf at a depth of 32 m (12.6°S) indicates that east waves prevail in the spring and summer with significant heights between 1 m and 2 m and periods between 6 s e 8 s. In autumn and winter SE waves are more frequent, with significant heights between 2 m and 3 m and periods between 6 s e 10 s (Pereira et al., under review). Highest wave height and period were 4 m and 17 s.

Data Analysis and Processing

Sea-level data was recorded by the IBGE tidal station located at the Coast Guard pier about 150m from the shore where a GNSS station is located. The tidal station was instrumented with an acoustic Aquatrack 4100 sensor with a recording interval of 6 min between November 2004 and December 2008. In April 2008 the acoustic sensor was replaced by a sonic Vegapuls 62 RADAR and a Sutron Encoder SDR with recording intervals of 1 minute and 5 minutes, respectively (IBGE 2021). This station is part of the GLOSS network (station number 334) and hourly data is made available both by the IBGE Permanent Geodesic Tide Gauge Network (RMPG) and by the University of Hawaii Sea level Center (UHSLC) (Caldwell et al. 2015).

Research-quality data from UHSLC was obtained for the period 01/01/2005 to 31/12/2018, complemented by a Fast-Release time series to December 2024 (Cadwell et al. 2015). The time series accessible at IBGE extends from January 2004 to December 2023. When comparing the UHSLC and IBGE time series small differences in weekly-to-monthly MSL were detected. That was especially the case with the Fast-Release data that caused phase angles of semi-diurnal constituents to deviate a few degrees from preceding values. With the aid of harmonically reconstructed time series, careful considerations were made between the two data sets in order to produce a complete time series between 2004 and 2024, totaling 21 years of data.

The data was interpolated to 10 minutes interval with a spline function in order to make tidal asymmetry calculations possible, and was reduced to the local Navy Hydrographic Center reduction level (RL) that is used as a reference level for nautical charts and tide tables. Locally, the RL is 2.286 m below the MSL and 0.122 m below the tidal staff zero, which is the refence for the GLOSS water level data.

The sea level signal was band-passed between cut-off frequencies of 1/53 hours and 1/720 hours (~1 month) to eliminate both subtidal and seasonal oscillations, respectively. The cut-off periods correspond to the inertial period at this latitude (of 53 hours) and the longest subtidal wave period identified by previous studies (Freitas et al. 2021). Height and period of subtidal oscillations were calculated using the upward zero-crossing method.

Trend analysis of the time series was performed with Mann–Kendall and Sen's slope tests. The former statistically tests whether there is an upward or downward monotonic trend over time, whereas the latter calculates the magnitude and direction of the identified trend. The trends were statistically tested considering a 95% confidence interval.

Harmonic analysis was performed with the T_TIDE package (Pawlowicz et al. 2002) to investigate the variability of diurnal and semi-diurnal components. Because of T_TIDE difficulties in dealing with very long time series, the extraction of the harmonic components for the 21-year time series was performed with the U_tide Matlab package (Codiga, 2011).

Calculations of tidal asymmetry were executed both through rise/fall ratio of each tidal cycle (values higher than 1 indicate faster falling tides) and through the phase and amplitude relationships between M2 and M4 tidal components, according to M4/M2 and 2(M4-M2), respectively. Higher ratios are associated with larger distortion of the tidal wave, whereas phase differences between 0° and 180° (180° and 360°) indicate faster rising (falling) tides (Friedrich and Aubrey,1988). Given the (small) range inequality between successive tidal cycles, tidal ranges were calculated between low and high tides (TRLH) and between high and low tide (TRHL). Water level duration curves were calculated annually using elevation classes between 0.4 m and 3.89 m with increments of 0.1 m. The curves were normalized in 2.5% intervals using a piecewise cubic interpolator (PCHIP). The statistics for spring and neap tide ranges considered the range of 5 cycles centered at the highest and lowest tidal range, respectively, in the spring-neap cycles.

Information on atmospheric pressure were obtained from a station maintained by the National Meteorologic Institute (INMET - https://portal.inmet.gov.br) located close to the BTS entrance from 2005 to 2024 (Figure 1). The hourly data was subjected to quality-control analysis, with spurious data identified as values higher(lower) than the 6- hours mean (centered at the time of interest) plus(minus) 2 times de standard deviation (Emery e Thompson, 2004).

Wind data was downloaded from the Cross-Calibrated Multi-Platform (CCMP - https://www.remss.com), a 6-hours interval combination of ocean surface 10m wind retrievals from multiple types of satellite microwave sensors and a background field from reanalysis, with a spatial resolution of 0.25°. A time series of north (vN) and east (vE) velocities was extracted from a grid element closest to shore centered at 13.125°S and 38.125°W (Figure 1). This grid element is the closest to METAR (SBSV) meteorological station (useful data from 2009 onwards) and to the SiMCosta BA1 buoy (data from 2019 to present), which were used to ground-truth the CCMP data set. A preference for CCMP data was given for it covers the whole tidal time series and because of existing bias at the METAR and SiMCosta records caused by the terrain. While the former underestimates S and SE winds, the latter underestimates E and NE winds. The alongshore wind component, responsible for the shore-normal Ekman transport, was calculated according to $V = -vE \sin\theta + vN \cos\theta$ where θ is the coastline orientation (-40° in the immediate region). Both the wind speed and atmospheric pressure were low-pass filtered using a cut-off period of 53 hours.

On 8 February 2024 the region was subjected to extensive tidal flooding, when the crest of a subtidal wave coincided with an equinox-spring tide at a time closer to the lunar perigee. Innumerous events of flooding and beach erosion were reported by the media in Salvador and other 30 coastal municipalities, including those located inside the BTS. The tide table published by the Navy Hydrographic Center (https://www.marinha.mil.br/chm/tabuas-de-mare) predicted a

maximum spring high-tide level of 2.8 m (relative to RL) for February 8, which will henceforth be taken as a reference elevation for coastal inundation.

A high-resolution LIDAR topography of the metropolitan area of Salvador (SEFAZ, 2017), carried out between 2016 and 2017 with a spatial resolution of 1:1000, was used to identify areas between the BTS entrance and Baia de Aratu (Figure 1) that are prone to submersion by high tides. The LIDAR vertical datum is the MSL at Imbituba Harbor (IMB datum - a national vertical datum established by IBGE), which is 0.86 m above the local RL. Elevation classes defined by the tidal datums Mean Water Level (MWL), Mean High-water Neap (MHWN), Mean High Water (MHW), Mean High-water Spring (MHWS) and Maximum High-water Level (MHL) were drawn along the shoreline.

A numerical simulation of the bay hydrodynamics was used to assess the propagation of subinertial waves inside the BTS. A Regional Ocean Modelling System (ROMS) was implemented in the region with two nested meshes (Figure 2a) (Franklin et al. under review). The higher-resolution mesh covered the whole bay and neighboring shelf with grid spacing varying between 200 m and 50 m (Figure 2b). Hourly solutions between 2008 and 2021 were forced using global winds from CFSR, contour conditions from Glorys-Mercator and initial conditions from HYCOM. As additional boundary conditions daily-mean discharge of 43 rivers, 15 of them debouching into the BTS, were included. Data from gauged rivers were obtained from the National Water Agency website (ANA). For smaller, unmonitored rivers, discharge was estimated using area-discharge relationships with the nearest gauged river. Validation of the hydrodynamic simulation is provided as supplementary material.

Tides were imposed at the model open boundary through the main harmonic components (M2, S2, N2, K2, K1, O1, P1, Q1) from TPXO 8.0 (Egbert e Erofeeva 2002), with a spatial resolution of 1/12th degrees. The grid bathymetry was obtained from a blend of ETOPO (Amante and Eakins 2009) with very high-resolution nautical charts produced by the Brazilian Navy (https://www.marinha.mil.br/chm/dados-do-segnav/cartas-raster), whose scales varied from 1:350,000 in the continental margin to 1:8000 inside the bay.

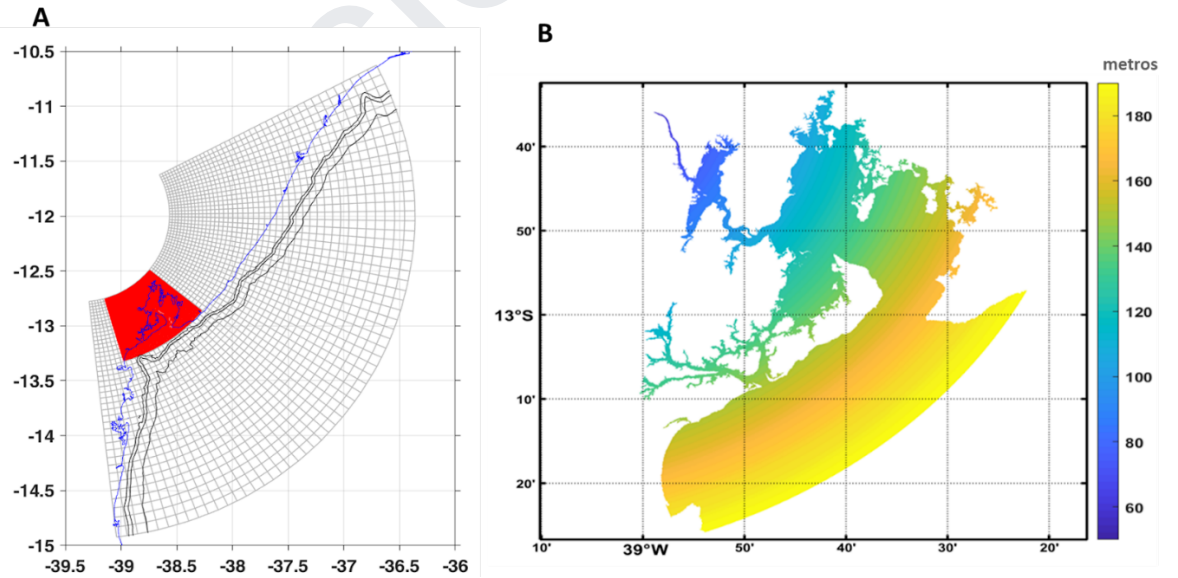

Figure 2 – The domain of the two nested numerical grids used in ROMS (A) and the variable spatial resolution of the higher-resolution grid (B).

Five sites were chosen to validate the model results (dark stars in Figure 1), one coincident with the IBGE tidal station and four others in more internal positions where tidal records exist. A comparison of the observed and simulated time series is presented in Figure 3. Correlation coefficients are higher than 0.98 for all stations, with RMSE of 0.08 m in Salvador, 0.09 m in Aratu channel, 0.16 m in Madre de Deus and 0.15 m in Itaparica channel. In Salvador and Aratu channel the error corresponds to 4% of the spring tidal range, whereas in Madre de Deus and Itaparica Channel it corresponds to 6% of the spring tide range of the compared time series. Higher errors at the two inner stations are ascribed to the limitation of the numerical grid to reproduce the complex bathymetry around Madre de Deus and to the low-resolution nautical chart (1:60,000) that covers Canal de Itaparica (Franklin et al., under review). A complete validation of the numerical model can be found in Franklin et al. (under review).

To investigate the propagation of subtidal oscillations five sites were chosen in the model grid (red dots in Figure 1) which are representative of the inland most urban centers around the bay. We used the time series of 2020 for this analysis, a year with a higher frequency of larger subtidal oscillations. The elevation difference between simulated high-tide and the high tide obtained from the reconstituted tidal oscillations provided a measure of the coastal flooding.

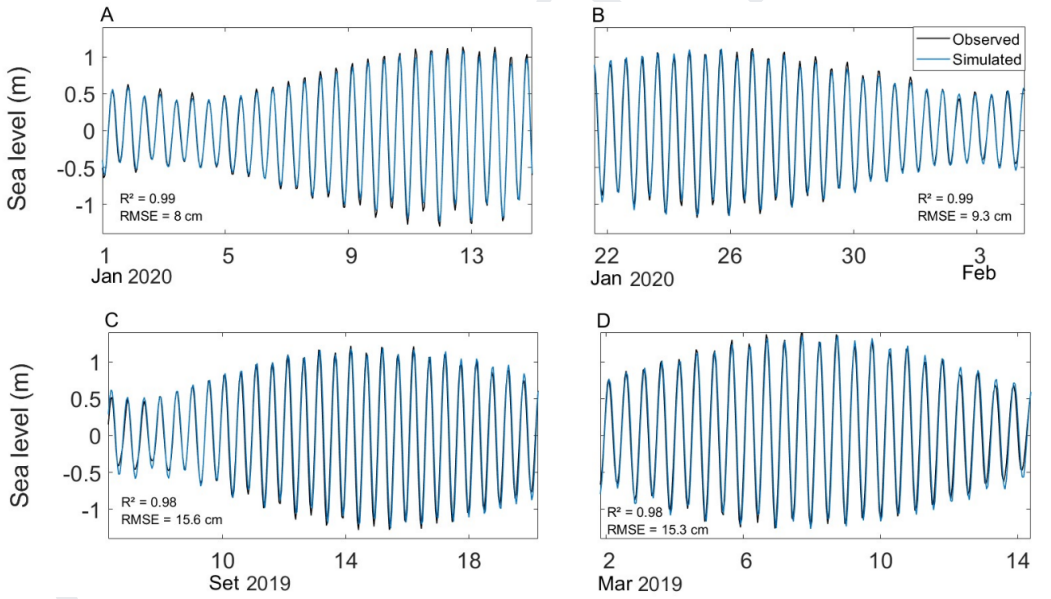

Figure 3 – Observed (black) and simulated (blue) sea level variation at 4 sites within the BTS. Correlation indices (R) and the root-mean squared error (RMSE) is indicated for each site. A) IBGE station, B) Aratu, C) Madre de Deus, and D) Matarandiba.

RESULTS

The complete water level time series is shown in Figure 4a. Minimum, maximum and mean

water levels were -0.11 m (September 2015), 3.02 m (April 2024), and 1.43 ± 0.62 m, respectively (Table 1). MHWS and MHWN were 2.58 ± 0.14 m and 1.94 ± 0.12 m, respectively, whereas MLWS and MLWN were 0.30 ± 0.13 m and 0.96 ± 0.10 m, respectively (Table 1).

The water-level duration curve (Figure 5a) shows that for 50% of the time the water level was below 0.88 m or above 1.9 m, with a median value of 1.37 m. However, these frequencies underwent an increasing trend over the 21 years, as indicated by the curves representing 2004 and 2022, whose median values are 1.35 m and 1.41 m, respectively. The trend is more evident if the annual variation of higher percentiles is considered. Figure 5b shows the trends progressively increase from 2 mm/yr to 3 mm/yr between the 50th and 99th percentile, accounting for respective total increases of 4.2 cm and 6.3 cm in their elevation over 21 years. Figure 5b also shows a 4-years modulation that becomes more conspicuous at the higher percentiles, attaining 5 cm in amplitude at 99th percentile.

Seasonal variations in the water level are well-established, with lower sea-levels in spring and summer and higher sea levels in the fall and winter (Figure 4d). The seasonal amplitudes fluctuate between 14 cm and 18 cm. This seasonality is well explained by variations in the wind direction (Figure 4e), with a correlation coefficient of 0.61. During the spring and summer, the wind blows southward (negative values) causing an offshore Ekman transport that lowers MSL. Conversely, winds blowing northwards in the fall and winter push water against the coast and elevate the MSL. The correlation index is significantly lowered, down to 0.29, when the mean-annual MSL and wind are analyzed. Monthly-mean air pressure is not correlated with MSL (Figure 4f). However, annual-mean values show a negative correlation of -0.69, indicating that the inverse barometer effect plays a role in the interannual MSL variability.

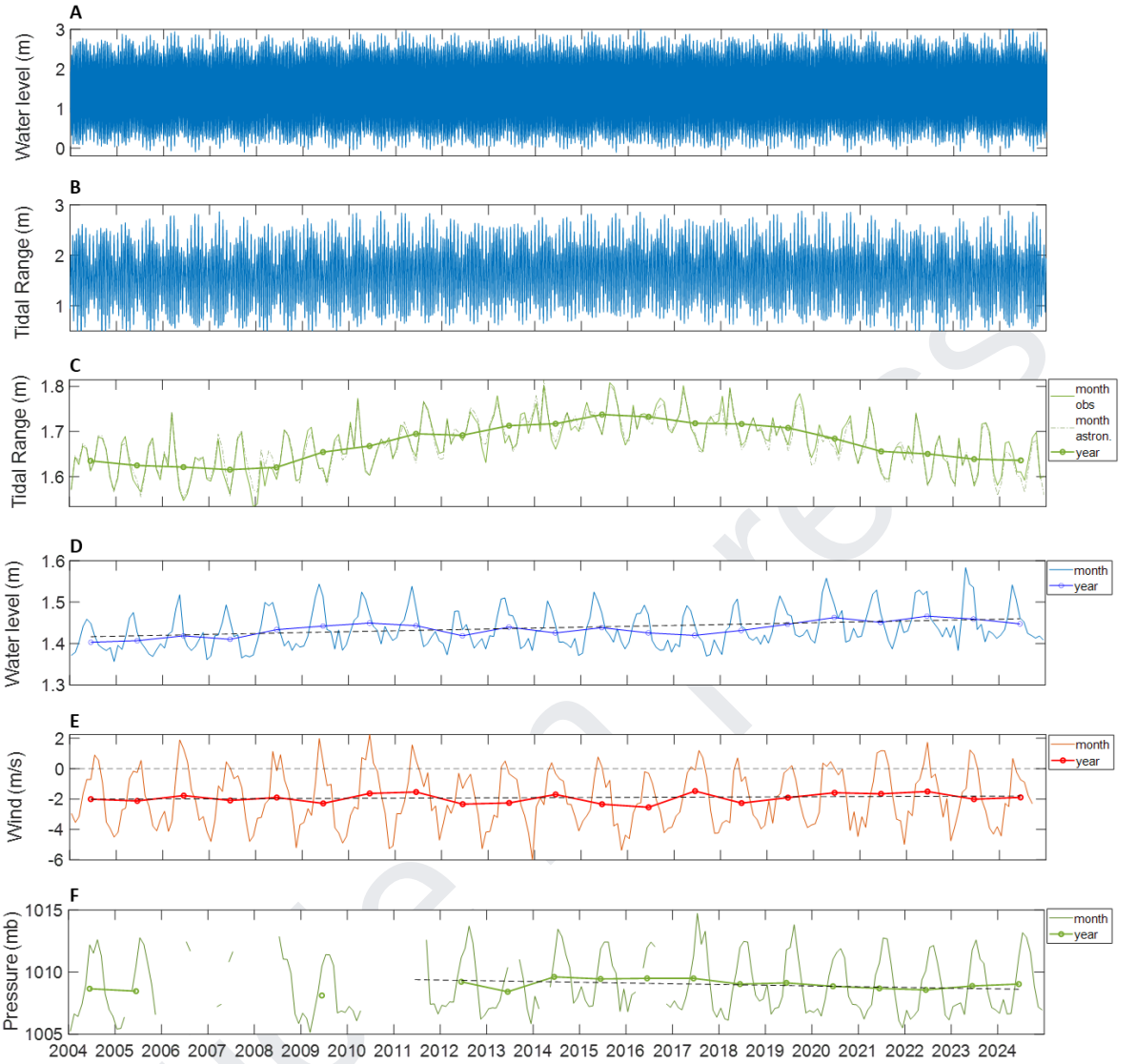

Figure 4 – Time series of the tides at IBGE station (A), tidal range of each tidal cycle (B), monthly- and yearly-mean tidal ranges (C), monthly- and yearly-mean sea levels (D), monthly- and yearly-mean alongshore wind speeds from CCMP (E), and monthly- and yearly-mean air pressure from INMET - Salvador station (F). Months or years with less than 80% of the valid data were not included.

The mean tidal range was 1.67 m ± 0.52 m, varying from a minimum of 0.44 m (October 2004) to a maximum of 2.88 m (September 2019) (Figure 4b). The mean, minimum and maximum spring tidal ranges were 2.28 ± 0.06 m, 1.65 m and 2.88 m, whereas the respective neap tidal ranges were 0.98 ± 0.08 m, 1.55 m and 0.44 m (Table 1). The frequency distribution of tidal ranges is bimodal (Figure 5c), with most frequent ranges being 1.2 m and 2 m, which correspond to the 25th and 75th percentiles (Figure 5d). Mean spring and neap tide ranges are 2.31 m ± 0.19 m and 0.96 m ± 0.16 m,

respectively. Differences between low-to-high tide range and high-to-low tide range can reach 0.4 m either way (Figure 6), but are modulated by fortnight, monthly, semi-annual and annual cycles. Larger high-to-low tide ranges (negative values in Figure 6) tend to occur at high spring tides, an additional forcing agent to the documented ebb-dominance of tidal currents (Cirano and Lessa, 2007).

Table 1 – Characteristic tidal range values for the Salvador Harbor tidal station in relation to the local hydrographic datum (RL) and Imbituba datum (IMB), which is the national vertical datum.

Datums	Elevation (m) RL	Elevation (m) IMB
HWL	3.02	2.16
MHWS	2.58 ± 0.14	1.72
MHW	2.28 ± 0.27	1.42
MHWN	1.94 ± 0.12	1.08
MWL	1.43 ± 0.62	0
MLWN	0.96 ± 0.10	
MLW	0.60 ± 0.27	
MLWS	0.30 ± 0.13	
LWL	-0.11	
	Tidal Ranges (m)	
Mean tidal range	1.67 m ± 0.52	
	Spring	Neap
Mean range	2.28 ± 0.06	0.98 ± 0.08
Max range	2.88	1.55
Min range	1.65	0.44

The annual mean-sea level between 2004 and 2021 rose at a linear rate of 2.15 mm/yr, as indicated by the dashed black line in Figure 4d, or at a rate of 1.85 mm/yr if monthly means are considered. The mean-annual values indicate important interannual oscillations. MSL rose between 2004 and 2010, lowered between 2010 and 2017 and rose once more until 2024, resulting in linear trends of 7.82 mm/yr, -3.71 mm/yr and 4.80 mm/yr, respectively, although the last two are not statistically significant. Wind velocity showed a very small, positive but not statistically significant trend of 0.01 m/s.yr, and air pressure presented a negative, but also not statistically significant, trend of -0.059 mb/yr. Both of these trends would assist a rising sea level.

The influence of equinox tides is clearly seen in Figure 4bc, with two peaks of tide range occurring every year. The ranges show a long-period oscillation associated with the nodal cycle (Figure 4c), with the annual-mean tidal range increasing 0.12 m between a minimum in 2007 and a maximum in 2015. The linear sen-slope fit on the yearly-mean data indicates the tidal ranges are increasing by 1.2 mm/yr, which amounts to 4 cm increase in 21 years.

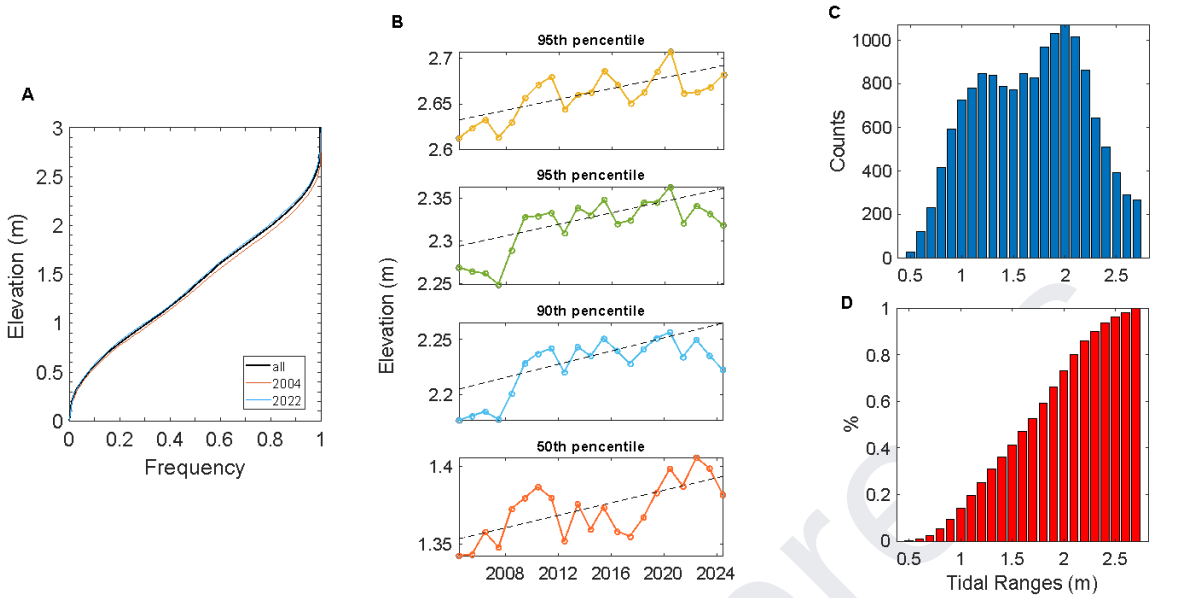

Figure 5 – Water level duration curve for 2004, 2020 and a mean curve for the 21 years of data (A). The variation of key percentiles of the sea-level cumulative-frequency distribution (B), the frequency distribution of tidal ranges (C) and its cumulative-frequency distribution (D).

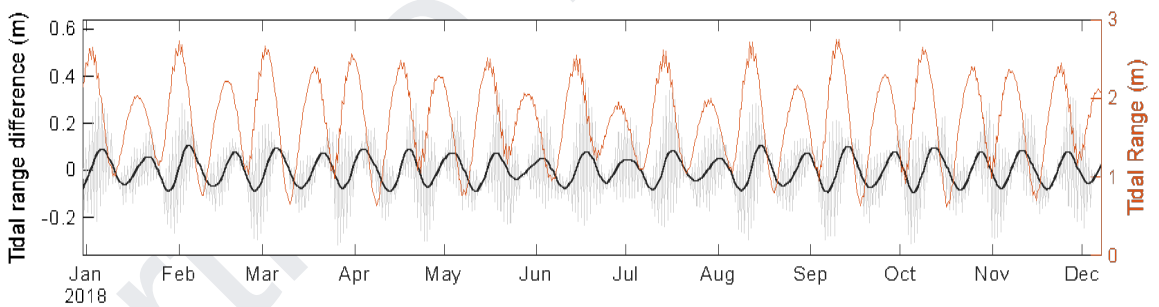

Figure 6 – Variation of the difference between low-to-high tide and high-to-low tide ranges for the year 2018. In gray the differences for each tidal cycle and in black the low-passed filtered signal with a cut-off period of 15 days. In red the range of each tidal cycle, highlighting spring-neap cycles.

Spectral analysis of the time series (Figure 7) shows the importance of overtides (M6, M4 and M3), semi-diurnal (M2, S2 and N2) and diurnal (K1, O1 and Q1) tides in the sea level variability. The red line in Figure 7 highlights the spectral peaks associated with the reconstituted astronomical tide, which explain 99.5% of the total water level variance. Important non-astronomical periodicity occurs at periods of 91.3 days, 2.3 years, 5.2 years and 10.5 years. The 91.3-days cycle is associated with the wind, which presents a distinct energy peak at the same frequency.

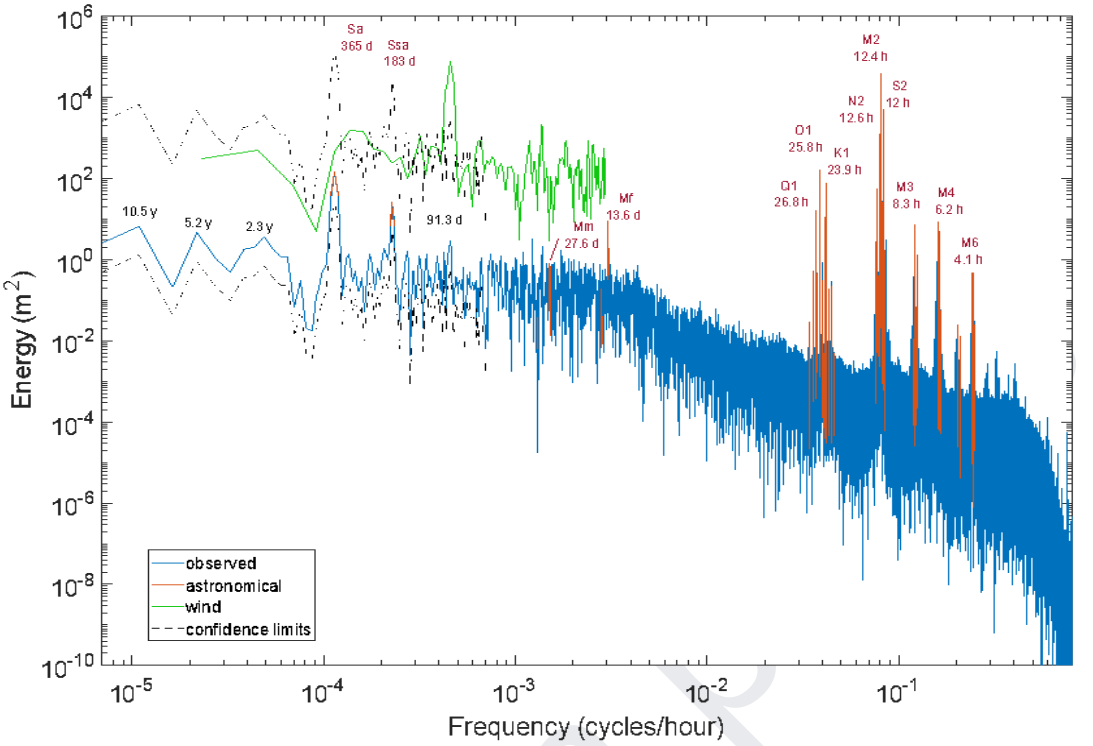

Figure 7 – Spectrogram of the observed and reconstituted astronomical tide at Salvador harbor based on 21 years of records. Main harmonic components are identified. The wind spectral density shows a correspondence with the sea level at the 93.3-days cycle.

The harmonic analysis of the whole time series resolved 68 constituents, and the most important ones for each periodicity class are shown in Table 2. The reconstituted astronomic tide accounted for 99.6% of the measured water level variance. On monthly basis it explained between 98% and 100% of the measured water level variance, with lowest and maximum monthly average values in solstice and equinoctial tides, respectively.

Eighteen semi-diurnal and twenty-two diurnal constituents account for 82% and 9%, respectively, of the total astronomic tidal amplitude. The overall tidal form-number is 0.09, but varied regularly with seasons associated with the sun latitudinal excursion. Smallest form-numbers, as low as 0.06, occurred in the austral fall equinox, whereas the highest values occurred in the winter solstices reaching up to 0.12 (not shown). This seasonal beating is forced by the out-of-phase oscillations of the semi-diurnal constituents and K1 (Figure 8), i.e., maximum semi-diurnal amplitudes are coincident with minimum K1 amplitudes. The monthly amplitudes of the four main tidal constituents oscillated between 0.72 m and 0.85 m for M2, 0.26 m and 0.43 m for S2, 0.04 and 0.09 for O1, and 0.01 m and 0.07 m for K1 (Figure 8). Statistically significant linear trend occurs with M2 amplitude only, that increased at a small rate of 3.2×10^2 cm/yr over 21 years.

Table 2 – Amplitude and phases (relative to local time) of important tidal harmonic constituents resolved from a 21-year record from Salvador Harbor.

Constituent	Amplitude (cm)	Phase (°)	Constituent	Amplitude (cm)	Phase (°)
SA	4.79	121	**MU2**	3.24	124
SSA	2.11	85	**N2**	14.60	109
MSM	0.14	202	**M2**	79.10	112
MM	0.40	359	**L2**	2.34	99.6
MSF	0.24	73.3	**S2**	31.20	127
MF	1.40	350	**K2**	8.94	121
Q1	1.76	94.8	**M3**	1.11	125
O1	6.36	124	**MN4**	0.39	185
P1	1.38	199	**M4**	1.19	269
K1	3.89	211	**MS4**	0.93	16.8
2N2	2.22	108	**M6**	0.30	353
NU2	2.62	104			

Monthly M2 phase angles varied by up to 7° over 21 years, with a minimum of 107° in December 2021 and a maximum of 114° in March 2008 (Figure 8). The M2 phase angle underwent a reduction of about 3° after 2019, but should be considered an artifact because it coincides with the transition between UHSLC and IBGE time series. Similar behavior is observed in the phase angles of the other constituents in Figure 8. The amplitude and phase angels of S2 and K1 show distinct seasonal cycles, varying respectively 0.2 m and 0.03 m in amplitude and almost 50° in the phase angle of both constituents.

The monthly M4/M2 ratio varied between 0.008 and 0.03, with annual maximum occurring mostly at the summer solstices (Figure 8). The monthly mean amplitude of M2 tend to be negatively correlated with M4 amplitude. The M4 and M2 phase angle difference oscillated around two modal values, 310° and 200°, the latter coinciding with the smallest M4/M2 ratios in the spring equinoxes. These phase-angle differences are close to 270° which is associated with the maximum tidal distortion favoring shorter falling tides. In fact, the mean, median, maximum and minimum rising/falling time ratio are 1.03±0.06, 1.02, 1.39 and 0.79, respectively. Figure 9 shows the natural logarithm of the rising/falling time ratio against the high-tide level. A logarithm representation is chosen because it produces a proportional graphical distribution of ratios around zero, with positive (negative) ratios indicating shorter falling (rising) tides. It is observed that positive log values are more numerous and the asymmetry intensity is modulated by the tide range, with larger asymmetries occurring during neap tides and smaller asymmetries during spring tides. The tidal oscillations tend to be more symmetrical at very large spring tides.

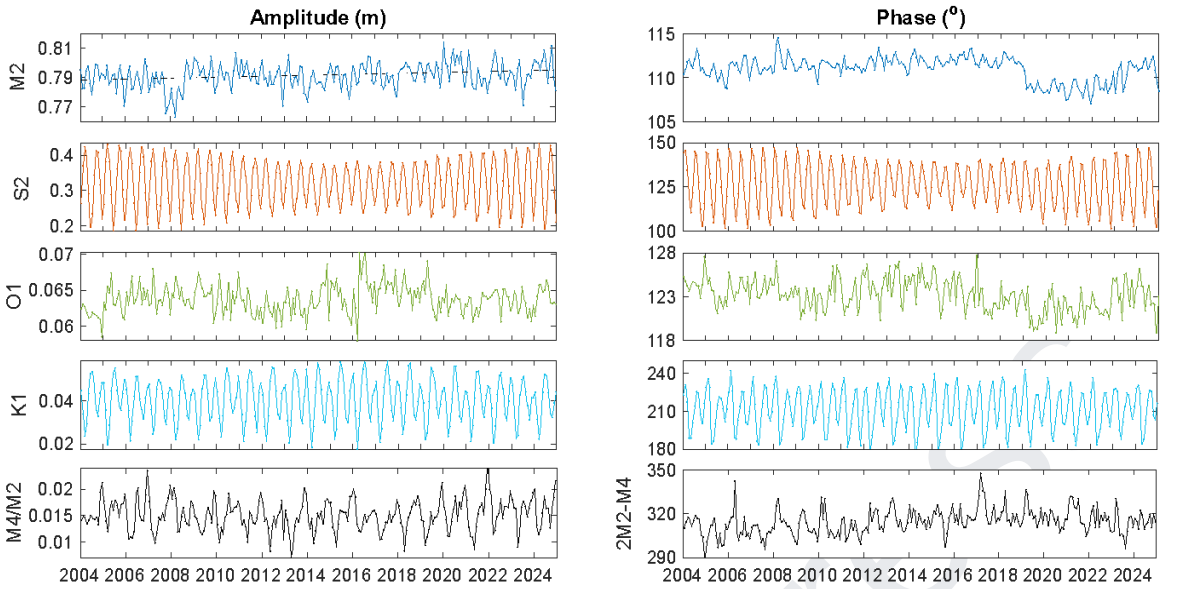

Figure 8 – Monthly variability of amplitude and phases of the main semi-diurnal and diurnal constituents, and the measures of intensity (amplitude ratio of M4/M2) and sense (phase angle difference 2M2-M4) of tidal distortion. Dashed line in M2 amplitude indicate the only statically significant linear trend.

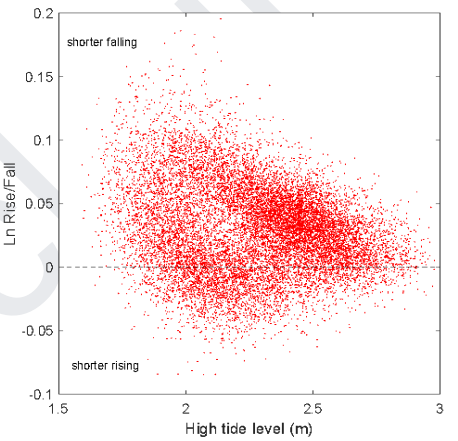

Figure 9 – Variation of the natural logarithm of the rising/falling time ratio against the high-tide level. Positive (negative) log values indicate shorter falling (rising) tide.

The monthly-mean ranges of the reconstituted astronomical tides differ by a maximum of 4 cm from those of the observed records, with the reconstituted tidal ranges averaging 3.5 cm less than those observed. Figure 10a shows the variability of this monthly difference along the 21 years, where seasonal cycles with larger positive differences occur in the austral summer. Subtidal sea-level oscillations (Figure 10b) reached up to 0.28 m, with periods varying between 2.2 days and 25.8 days. Wave height and period are positively correlated with a coefficient of 0.69 for the complete series and 0.88 for the annual mean. Mean subtidal wave height and period are 7.4 cm

and 9.7 days, respectively. A linear trend of 2.9x10^{-4} cm/yr for wave height and -0.1 days/yr for wave period, albeit not statistically significant, is suggested by the yearly means in Figure 10c, indicating that subtidal wave period might be decreasing concurrently with increasing wave height.

Figure 10 – A) Variability of the monthly-mean tidal range difference between the observed and the reconstituted astronomical tide, B) Variability of the height and period of subtidal oscillations and their annual-mean value (C).

As indicated by the water level frequency distribution in Figure 5, the severity of coastal inundation has been aggravated along the years. Figure 11a shows the monthly and yearly total amount of hours with water level above 2.8 m (the assumed threshold for coastal inundation), calculated both with the reconstituted astronomical tide and the observed tide. The threshold is overcome seasonally around the equinoctial tides, especially the austral fall equinox, with a maximum of 14 hours submergence in March 2020. The predicted submergence period tends to be smaller than the observed one, especially in the last 10 years. The observed total yearly hours were always higher than predicted, and more than doubled between 2006 (14 hours) and 2024 (32 hours). A cycle with approximately four years is clearly established in the length of inundation and in the maximum elevation of the mean spring equinoctial tides (Figure 11b), which also shows an increasing linear trend at a mean rate of 0.4 cm/yr, or a total of 8 cm in 21 years.

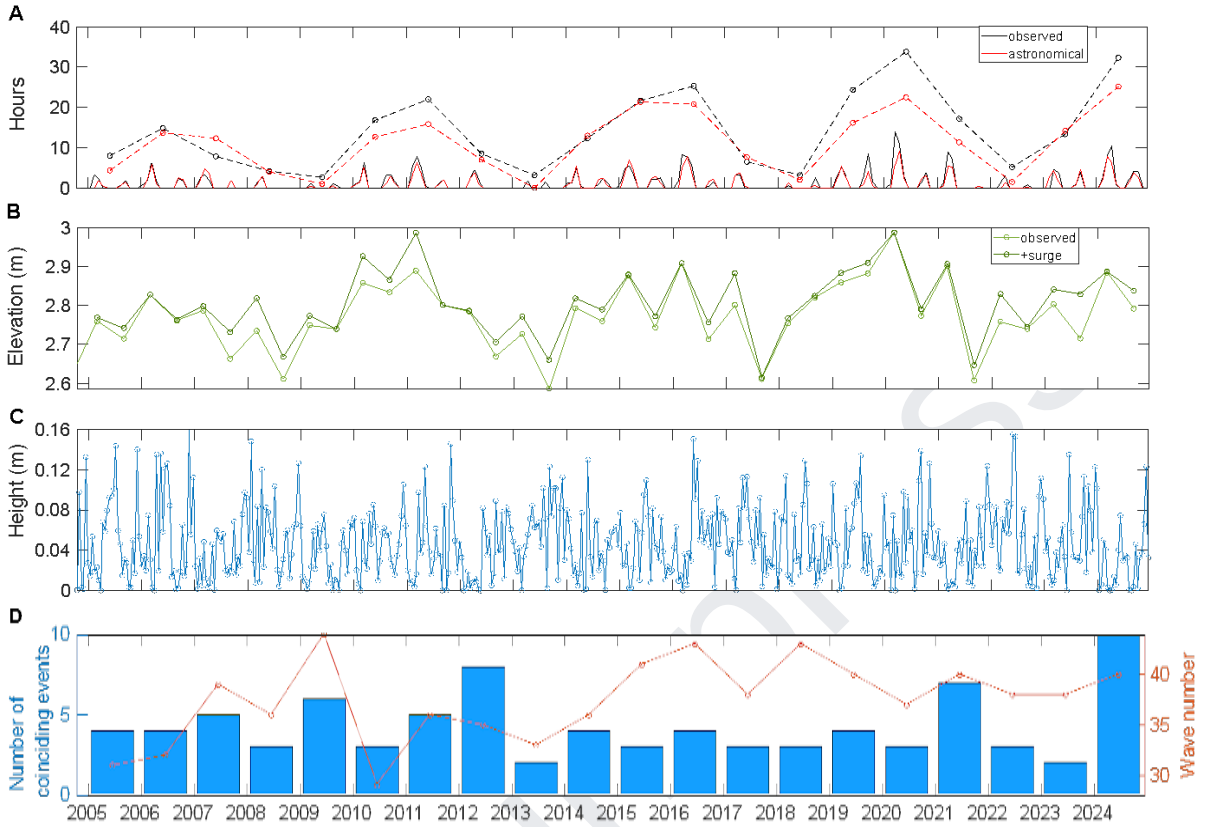

Figure 11 – A) Total of monthly and yearly hours with water level equal or higher than 2.8 m considering the observed records and the reconstituted astronomical tide. B) Maximum elevation of the observed mean spring equinoctial tides and the potential elevation in the case they coincided with the crest of the subtidal wave that occurred next to them. C) Elevation difference between the maximum surge elevation and the mean high water of spring tide cycles equal or above 2.45 m (90th percentile of the distribution). Positive values indicate potentially higher spring high tides. Zero values indicate spring tides were coincident with the maximum surge elevation (equals the bar graph). D) Numbers of storm surge events coincident with spring tidal cycles equal or above 2.45 m and total number of subtidal waves per year.

Subtidal sea level oscillations have become progressively more important as a driver for coastal inundation, as the difference between the predicted and observed extension of inundation indicates. The number of subtidal oscillations increased from 31 to 44 between 2005 and 2009, decreased to 29 in 2010 and then established a rising trend modulated by 3-to-4 years oscillations (Figure 11d). Very few of these waves occurred concurrently with spring tides reaching water levels above 2.45 m (very-high spring tides), which is the 90th percentile of the cumulative water level distribution (as shown in Figure 5). Figure 11c shows the elevation difference between the crest of the subtidal wave that occurred within a 14-days window centered at the very-high spring tide and the mean high-water level of that spring tide. Differences smaller than 1cm are associated with spring tides concurring with the crest of the subtidal waves, whose annual numbers are given by

the bars in Figure 11d. An average of 4 subtidal waves per year, or about 10% of the total number of subtidal waves identified per year (Figure 11d), coincided with very-high spring tides. The elevation difference indicates that the very-high tide levels could have been up to 16 cm higher if a coincidence occurred, raising the maximum elevation of several the mean spring equinoctial tides as shown in Figure 11b.

The effects of water level superelevation caused by subtidal oscillations appears to the aggravated landwards of the tide gauge station. Using the time series obtained from the numerical model at five stations around the bay (Figure 1), it is observed that the amplitude of the subtidal oscillations becomes larger landwards. Figure 12a shows the band-pass (53hs to 30 days) water level variation between February and May 2020 with 7 subtidal waves with maximum range of 21 cm in later March. The dashed black line shows the observed oscillations at IBGE station. Four of those waves grew in amplitude landwards, including the ones with larger amplitudes in March. Differences between simulated and predicted, with harmonic analysis of simulation results, high-tide elevation (Figure 12b) shows that high-water superelevation increased landwards (positive differences), reaching a maximum at Maragojipe where the high-tide level was 28 cm higher than predicted on March 28. Negative differences occur eventually at the trough of waves.

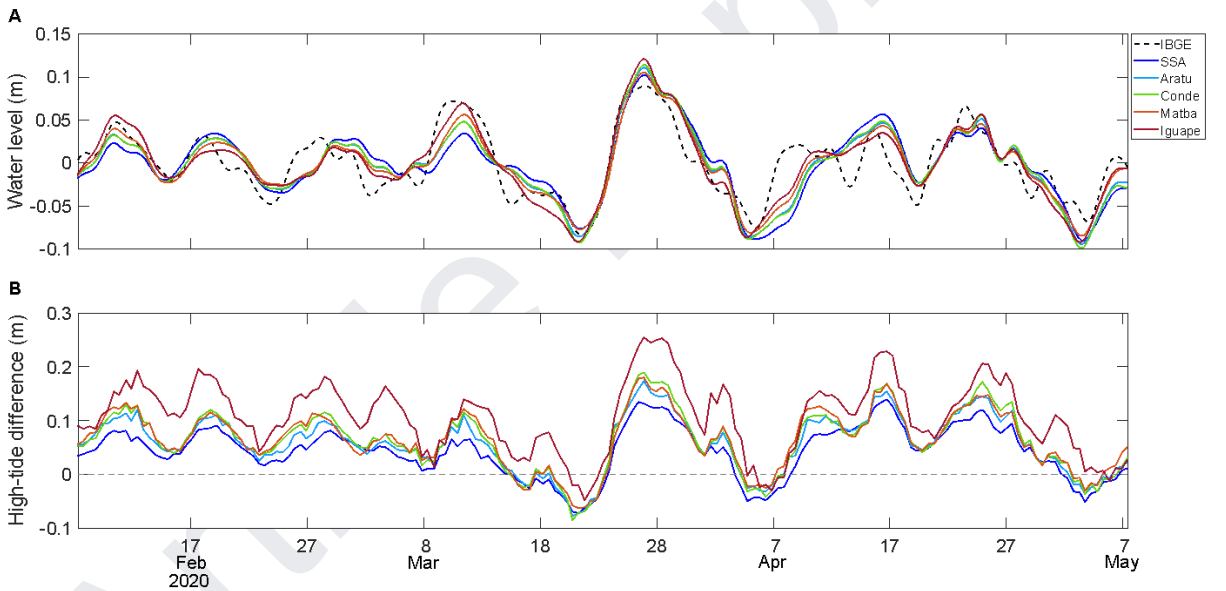

Figure 12 – A) Low-pass filtered water levels at IBGE tidal station and simulation results from 5 different sites. Simulation results from site SSA correspond do the observed IBGE time series. B) High-tide level difference between the simulated time series and the reconstituted astronomical high tide based of harmonic analysis of the simulation results for each site inside the BTS.

The LIDAR data indicates that coastal inundation of urbanized areas occurs mostly as a narrow band along the shoreline (Figure 13a), covering an area of 0.497 km^2 with elevations above MWL. The large majority (84.6 %) of the inundation occur in areas above 1.72 m in elevation, or above MHWS (Table 3), as clearly indicated by large expanses of this altitudinal class in Figure 13. About

three quarters of all inundation areas (0.375 km^2) are located on the margins of Baía da Ribeira (Figure 13bc), where 79% of the whole area between MHWS and MHL is located. Again, inside this small bay the highest elevational class prevails.

454 Tabel 3 – Distribution of the inundation area between tidal datums above MWL

Elevation (m)	Datuns	Whole Area (m^2)	(%)	Baía da Ribeira (m^2)	(%)
0 - 1,08	MWL - MHWN	37632	7.6	8920	2.4
1,08 - 1,42	MHWN - MHW	3176	0.6	3003	0.8
1,42 - 1,72	MHW - MHWS	35713	7.2	31372	8.4
1,72 - 2,16	MHWS - MHL	419992	84.6	332030	88.5

455

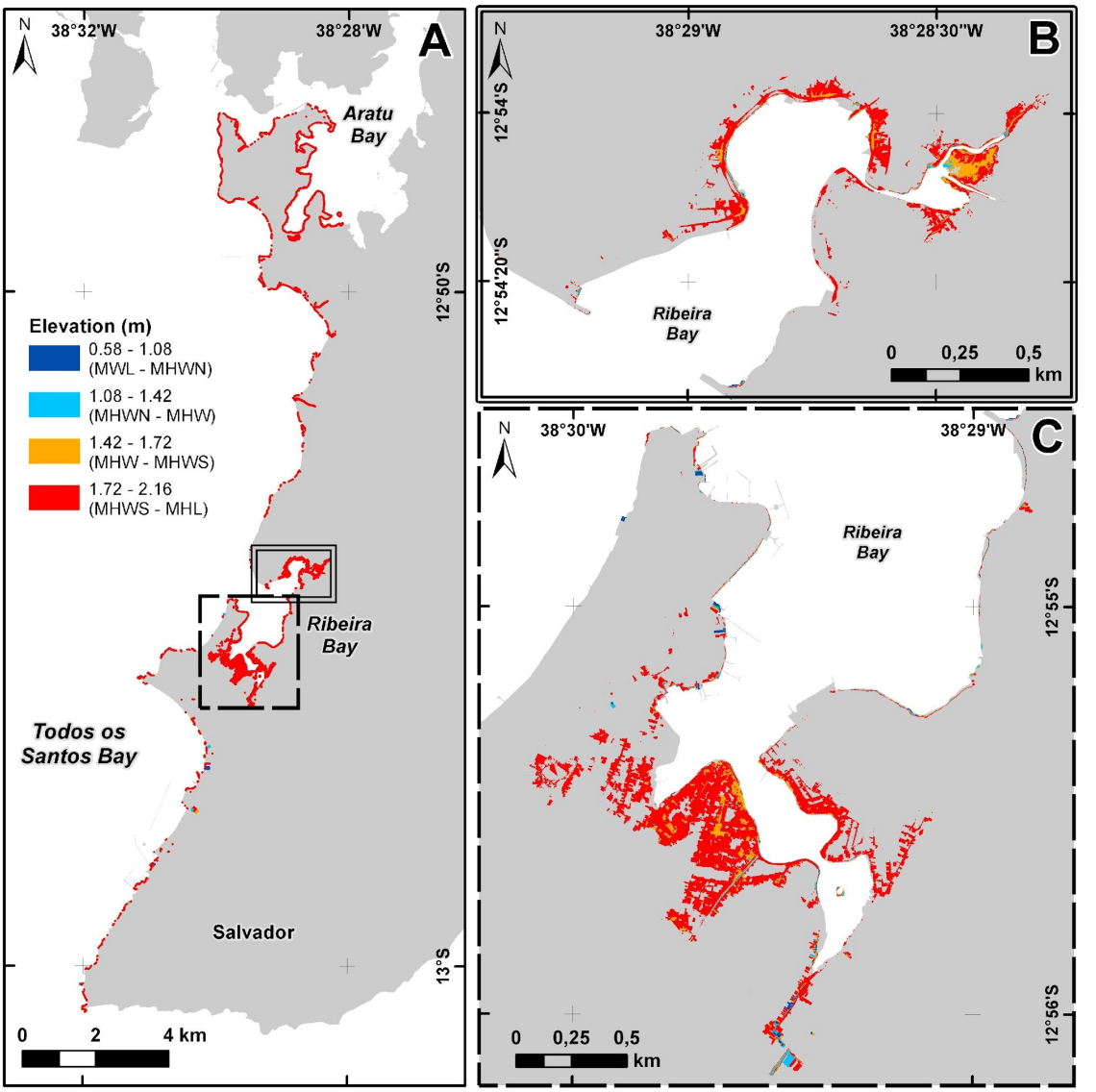

456

457

458 Figure 13 – Urbanized areas undergoing inundation along the Salvador bay shores at different
459 elevational classes (A). Detail of Baia da Ribeira southern and northern segments. Ground
460 elevation from LIDAR measurements (SEFAZ, 2017).

DISCUSSION

The astronomic tide in Salvador accounted for at least 98% of the monthly water level variance, and explained 99.6% of variance of the whole time series, implying very small influence of subinertial sea-level oscillations. In fact, subinertial oscillations larger than 0.2 m high, which correspond to 8% of the mean tidal range, account for only 1% of the total number of subinertial oscillations in the record. The subinertial oscillations in Salvador are almost 10 times smaller than those reported in south Brazil. Vianna et al. (2020) reports low-frequency waves of 1 m in Imbé (RS – 30°S), Trucollo et al. (2004) informs on subtidal oscillations with ranges of up to 0.9 m in São Francisco do Sul (26.25°S), and Schettini et al. (2019) tells a maximum range of 0.85 m in Santos (24°S). A study on the meteorological tides along the Atlantic coast of South America by Melo Filho (2017) shows a strong south-to-north reduction in the importance of subtidal oscillations on the water level variance between Rio Grande (32°S) and Fortaleza (3.6°S), from an astonishing 76% in the former to 0.2% in the latter. This trend is a consequence of reduced wind and atmospheric pressure disturbances towards lower latitudes, of increasing tidal amplitude away from an amphidromic point close to 32°S, and the energy loss associated with the propagation of the subinertial waves away from subtropical latitudes where cyclogenesis is frequent. Freitas et al. (2021) show that shelf-wave amplitude is dampened north of 22°S due to an increasing morphological complexity of the continental shelf, but especially north of 15°S after the shelf considerably narrows.

Coastal flooding becomes sporadic where subtidal oscillations are only a fraction of the tidal amplitude, such as in the north and northeast Brazil. At these sites coastal flooding tends to occur with equinoctial spring tides, limited to moments around high tide. This is because large tidal ranges, or swift changes in water levels, reduce the frequency that water levels will stay above inundation thresholds. Sweet and Park (2014) showed that San Francisco (37°N), with mean greater diurnal range of 1.9 m, is up to 5 times less likely to undergo coastal inundation than Galvestone (29°S), where the mean greater diurnal range is 0.62m.

Salvador does not show an increase in the number of inundation events over the years, with a maximum of 15 events about every four years. This ~4-year cycle is related to the association of the monthly tidal constituent MM and the semi-annual solar constituent SSA, the former associated with perigee-apogee cycle and the latter with the latitudinal transit of the sun. As the mean longitude of perigee crosses the equator, lunar perigean, lunar declination and solar equinox act along to reinforce spring tides. As perigee precesses through its 8.85-year cycle, it passes one of the equinoxes twice during the cycle, generating a 4.4-year periodicity (Ray and Merrifield, 2019). This tidal modulation that can greatly influence coastal inundation is largest along the northeast Brazilian coast with amplitudes varying between 4 and 6 cm, but almost non-existent along the coast of Rio de Janeiro according to Ray and Merrifield (2019) (Figure 14).

Although the number of inundation events per year have not increased, the submergence interval in the apex of the 4-years cycle was augmented in 20 hours per year between 2006 and 2020/2024. This is explained by a higher number of subinertial oscillations occurring in this latitude, especially in those years when the astronomical tidal forcing was at its maximum. Also to be considered is an apparent increasing trend in the amplitude of subinertial oscillations. More frequent subinertial oscillations can be ascribed to a positive trend in storminess in southwestern

South Atlantic. Conrado et al. (2024) showed a positive, statistically significant storminess trend between 20oS and 35oS in the 1900-2010 reanalysis data from ERA20C, a trend that is maintained when analyzing a more recent 1970-2010 period. In line with these results, Gramcianinov et al. (2023a,b) found an increase of significant surface wave height and wave period using ERA5 reanalysis results between 1993 and 2021 in the same area. It is also possible that the local action of storm winds in supra-inertial frequencies may cause a storm surge that concurs with the crest of a subinertial oscillation. This potential synergy has not been investigated and is a venue for further studies.

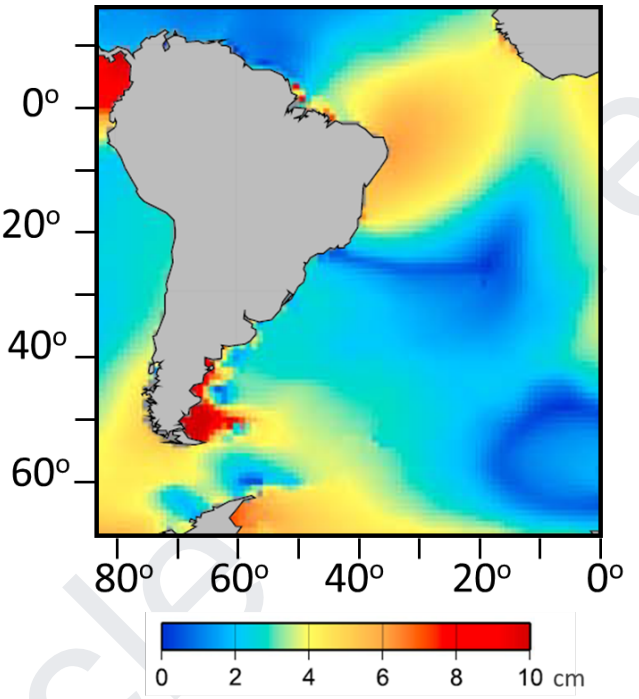

Figure 14 - Amplitude of the 4.4-year modulation of extreme tidal high water (modified from Ray and Merrifield, 2019).

Coastal inundation of the suburban area of Salvador on the margins of Baía da Ribeira, on pre-existing mangrove areas extensively reclaimed between the 1950's and 1980's and whose removal reduced the bay area by 43% (Franklin and Lessa 2011). This area covers 0.375 km^2 of neighborhoods with a population of ~109,000 (IBGE Census 2022), and a population density of 372 inhabitants/km^2. It has already been mapped as a suburbia with the highest risk of submersion by rising sea levels (Nicolodi and Petermann, 2010). The mapped are likely larger in the northern sections due to the landward tidal amplification in the bay, *i.e.*, the reference elevation from Salvador used in the analysis underestimates the tidal flooding in more internal parts of the bay. Because high tide levels hamper the drainage of pluvial waters, and knowing that extraordinary high tide levels are commonly associated with storm surges, the potential extent of tidal inundation is deemed to be worsened with a compound flooding, or the damming of pluvial waters. For

instance, it is suggested that the synergy between these phenomena in Macau increases the inundated area by 19% and cause the underground drainage to backflow for 1.4 km away from the coastal boundary (Gao et al. 2023).

The increase in the amplitude of subtidal waves as they propagate into the BTS may aggravate coastal flooding scenarios in low-lying areas further inland. The exacerbation of the high-tide elevation would be up to 5 centimeters higher than that experienced in Salvador at all of the sites investigated (Figure 12), except for the innermost site inside at Iguape Bay, where superelevation would be almost 15 cm higher than that in Salvador. Similar behavior is reported for large convergent estuaries where flow impedance at the inlet is not significant and tides are amplified upstream (Lyddon et al. 2019; Spicer et al. 2019), such as in the BTS. Spicer et al. (2019) shows that in inland estuarine regions where river discharge becomes progressively more important, high-tide superelevation is intensified due to damming of the river flow. This phenomenon would help to explain higher high-tide elevation differences in Maragojipe, where Paraguaçu River exits into the bay.

The amplitude of M2 tidal constituent increased at a rate of 3.2×10^{-2} cm/yr, totaling 0.6 cm over the observed years. This is coincident with the almost null trend found by Efraime et al. (2025) in Salvador. Differently from these authors, who found a negative trend of -0.48 mm/year in O1 tidal amplitude, our analysis found an almost null, albeit positive, increasing trend of O1 which was, however, not statistically significant. Must be born in mind that Efraime et al. (2025) analyzed a time series of 19 years (2004-2022), 1 year shorter than the series here analyzed. These small or non-existing trends in the tidal constituents in Salvador differ from positive trends of M2 amplitude in Imbituba (0.55 mm/year) and Ilha Fiscal (0.11 mm/year).

The lunar nodal cycle modulated the observed yearly-mean tidal range by 12.2 cm, 1.1 cm more than the modulation imposed on the predicted tides (11.1 cm). The impact of the nodal cycle on the astronomical monthly-mean high water was 7.3 cm, calculated after removing 4.4 years cycle with a Lanczos low-pass filter. This value is at least 2 times more than the nodal modulation found by Peng et al. (2019) in Cananéia and Rio de Janeiro, with corresponding ranges of approximately 2 and 1 cm. Maximum high-water elevation was reached in 2015 (Figure 4), coincident with other semi-diurnal tidal settings (Peng et al., 2019). More extensive coastal flooding in Salvador was recorded in 2020 and 2024 (Figure 11), which is closest to the trough of the nodal cycle. Therefore, graver coastal flooding events can be anticipated in 2034, the next peak of the nodal cycle.

Variations in wind speed is in agreement with the seasonal MSL variability. Alongshore winds blowing southward (negative speeds) lower the MSL in the summer, and rises MSL in the winter when blowing in the opposite direction (positive speeds). Variations in air pressure, on the other hand, opposes the seasonal MSL trend, with lower monthly mean air pressures in the summer, when MSL is at a minimum (Figure 4). However, interannual variation of the yearly mean air pressure correlates positively with the yearly-mean MSL. The observed positive wind velocity trend in the last 21 years, meaning weaker negative winds, and a negative trend of air pressure have apparently worked in tandem to assist progressively higher high-tide levels and coastal flood duration.

The local rate of sea-level rise has a strong meteorological component, mostly associated with the wind, responsible for large short-term deviations from the linear rising trend of 2.15mm/yr over 21 years, if yearly means are considered. A decreasing trend in negative wind velocities between

2004 and 2010 and between 2017 and 2024 are associated with the rising MSL trends, whereas increasing wind speed between 2010 and 2017 are correlated with a lowering MSL trend. Long-term sea-level rising rates are largely impacted by interannual and interdecadal variations (Ezer, 2013, Hamlington et al., 2019), especially in the more recent decades when the overall rising rate increased from 2.1 mm/y in 1993 to 4.5 mm/y in 2023 (Hamlington et al. 2024). Significant oscillations in basin-wide MSL can occur in a few years due to climate swings, such as the extreme El Niño event of 2015-2016 that caused a 15 mm rise in the global mean-sea level in 2 years (Llovel et al., 2023).

The MSL-rise rate of 1.85 mm/yr, obtained from the monthly mean water levels, is much smaller than the 3.1 mm/yr reported by Efraime et al. (2024), who analyzed a time series from Salvador IBGE station between October 2004 and December 2022. Their rate takes into account an approximately null vertical land movement according to the local GNSS station. If we analyze same time interval in our data, a rate of 2.07 mm/yr is obtained, still smaller than Efraime et al. (2024). The difference observed apparently resides in the data set used by both studies. While our time-series was centered on UHSLC data with the IBGE data set as auxiliary, Efraime et al. (2025) used the complete IBGE time series. Figure 15a shows the difference between the raw GLOSS and IBGE series for a representative short-time interval in 2010. It is observed an elevation misfit between the two series between October 23 and November 03, which is similar to misfits detected in other periods. Noticeable differences also occur in the computations of the monthly-mean sea-levels, especially between 2008 and 2015 (Figure 15b).

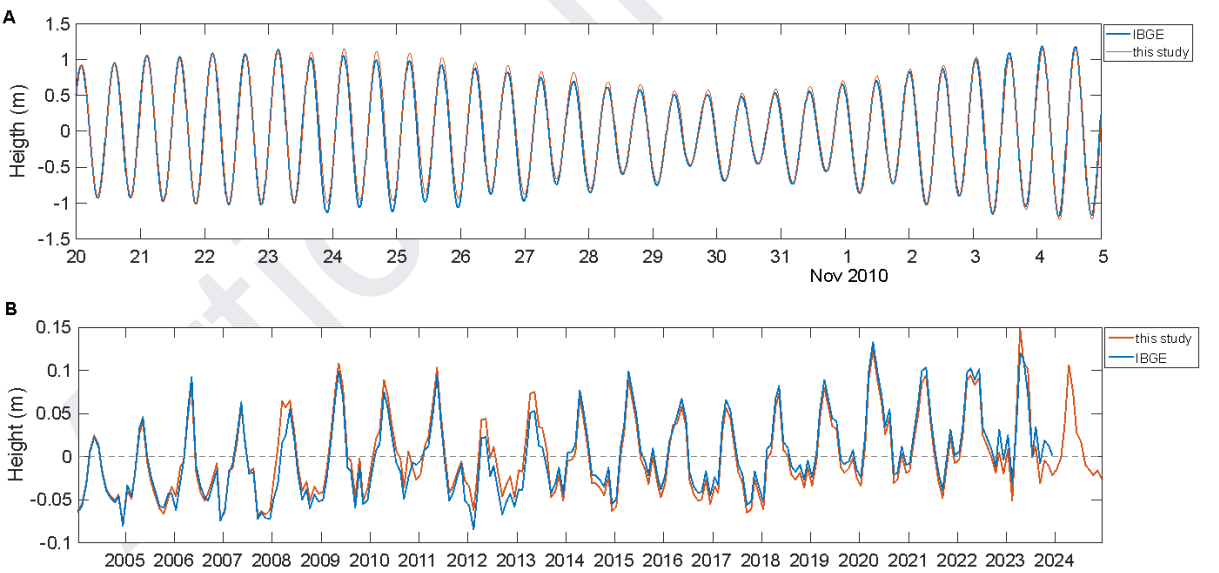

Figure 15 – A) A comparison of the IBGE and UHSLC water level time-series with a period of misfits between October 2023 and November 03. B) Monthly-mean MSL computed from the IBGE and UHSLC time series between 2004 and 2024.

CONCLUSION

The tides have the largest effect on sea level variability at the entrance of the BTS, with subtidal oscillations explaining less than 2% of the monthly or yearly sea level variance. The mean tidal range is 1.67 m, but ranges can vary 6-fold between the smallest and largest values within the tide-nodal cycle. The difference between maximum and minimum water levels recorded, or the maximum amplitude of intertidal levels, was 3.18 m, about 10% larger than the largest tidal range.

The mean sea-level increased at a linear rate of 2.15 mm per year between 2004 and 2024, albeit with significant interannual fluctuations associated with the wind speed: consecutive years with a trend of increasing (decreasing) negative wind speeds caused a negative (positive) trend in the MSL. Along with a long-term rise in sea level, a trend of increasing frequency and amplitude of long-period waves was detected. However, rising MSL had no apparent impact in changing the amplitude nor the phase of the main diurnal and semidiurnal tidal harmonic constituents.

The flooding of the Salvador coastal area inside the bay, associated with extreme water levels is largely restricted to a reclaimed mangrove area inside Baía da Ribeira. Inundation events occur every year, but significant ones take less often in association with the 4.4 years tidal cycle. Rising sea level and increasing frequency of sub-tidal waves have caused an amplification of inundation events. The number of hours with sea-level above the inundation threshold increased 3-fold over the last 2 years. Inundation events are likely worsened in the most internal part of the bay.

AI DISCLOSURE

We declare that no generative artificial intelligence (AI) tools were used in the preparation, writing, or editing of this manuscript.

DATA AVAILABILITY STATEMENT

The raw data analyzed is available at the University of Hawaii Sea level Center (UHSLC, station number 334, accessed through the link https://uhslc.soest.hawaii.edu/data/, and at the Brazilian Permanent Geodesic Tide Gauge Network, accessed through the link https://www.ibge.gov.br/geociencias/informacoes-sobre-posicionamento-geodesico/rede-geodesica/10842-rmpg-rede-maregrafica-permanente-para-geodesia.html?=&t=observacao-do-nivel-do-marrmpg

FUNDING

This study is a byproduct of the project 'Assessment and research of sun coral in Todos-os-Santos Bay', a cooperation agreement between UFBA and PETROBRAS (No 5850.0107361.18.9) regulated by R,D&I investment clauses of Brazilian Agency of Petroleum, Natural Gas and Biofuels (ANP Resolution 03/2015).

AUTHOR CONTRIBUTION

G.C.L: Conceptualization; Investigation; Methodology; Graphics; Formal analysis; Writing original draft, review & editing
G.L.P: Investigation; Formal analysis; Graphics; Writing
F.M.S.: Formal analysis; Graphics; Software
P.A.S.: Data curation; Resources
C.E.P.T.: Data curation; Software; Investigation
M.M.A.: Software; Resources

CONFLICTS OF INTEREST

The authors declare no conflict of interest

REFERENCES

Caldwell, P. C., Merrifield, M. A. & Thompson, P. R. 2001. Sea level measured by tide gauges from global oceans as part of the Joint Archive for Sea Level (JASL) since 1846 [Data set]. National Oceanic and Atmospheric Administration (NOAA) National Centers for Environmental Information (NCEI). doi: 10.7289/v5v40s7W.

Chen, W.-B. 2025. Gradual strengthening of global oceanic surface winds: Correlations with sea surface temperature and implications for wind power extraction. Heliyon, 11(4), e42788. doi: 10.1016/j.heliyon.2025.e42788.

Church, J. A. & White, N. J. 2011. Sea-Level Rise from the Late 19th to the Early 21st Century. Surveys in Geophysics, 32(4–5), 585–602. doi: 10.1007/s10712-011-9119-1.

Cirano, M. & Lessa, G. C. 2007. Oceanographic characteristics of Baía de Todos os Santos, Brazil. Brazilian Journal of Geophysics, 25(4), 363–387. doi: 10.1590/s0102-261x2007000400002

Codiga, D. L. 2011. Unified tidal analysis and prediction using the UTIDE Matlab functions. University of Rhode Island. Doi:10.13140/rg.2.1.3761.2008.

Daniel, E., Harari, J., De Camargo, R., Soares, S., Mascagni, M. L. & Filho, A. F. H. F. 2025. Sea level variation along the Brazilian coastline from the perspective of climate change. Regional Studies in Marine Science, 89, 104309. doi: 10.1016/j.rsma.2025.104309.

De Cai Conrado, E. T., Da Rocha, R. P., Reboita, M. S. & Cardoso, A. A. 2024. Cyclone Classification over the South Atlantic Ocean in Centenary Reanalysis. Atmosphere, 15(12), 1533. doi: 10.3390/atmos15121533.

Dodet, G., Melet, A., Ardhuin, F., Bertin, X., Idier, D. & Almar, R. 2019. The contribution of Wind-Generated waves to coastal Sea-Level changes. Surveys in Geophysics, 40(6), 1563–1601. doi: 10.1007/s10712-019-09557-5.

Egbert, G. D. & Erofeeva, S. Y. 2002. Efficient inverse modeling of barotropic ocean tides. Journal of Atmospheric and Oceanic Technology, 19(2), 183–204. doi: 10.1175/1520-0426(2002)019.

Emmery, W. J. & Thompson, R. E. 2004. Data Analysis Methods in Physical Oceanography.

671 Pergamon Press. doi: 10.1016/C2010-0-66362-0.
672 Ezer, T. 2013. Sea level rise, spatially uneven and temporally unsteady: Why the U.S. East Coast, the
673 global tide gauge record, and the global altimeter data show different trends. Geophysical
674 Research Letters, 40(20), 5439–5444. doi:10.1002/2013gl057952.
675 Franklin, T. S., Lessa, G. C., Teixeira, C. E. P., Santos, F. M., Marta-Almeida, M. & Mendes-Lopes, R.
676 2024. High-Resolution Simulations Of Coastal Dispersion of Tubastraea Spp. Larvae from a
677 Large Estuary in Northeast Brazil. SSRN Electronic Coral Reefs. doi:
678 10.1007/s00338-026-02817-y.
679 Freitas, P. P., Paiva, A. M., Cirano, M., Mill, G. N., da Costa, V. S., Gabioux M. & França, B. R. L. 2021.
680 Coastal Trapped Waves Propagation along the Southwestern Atlantic Continental Shelf.
681 Continental Shelf Research, 226, 104496. doi: 10.1016/j.csr.2021.104496.
682 Friedrichs, C. T. & Aubrey, D. G. 1988. Non-linear tidal distortion in shallow well-mixed estuaries: a
683 synthesis. Estuarine Coastal and Shelf Science, 27(5), 521–545. doi:
684 10.1016/0272-7714(88)90082-0.
685 Gao, L., Du, H., Huang, H., Zhang, L. & Zhang, P. 2023. Modelling the compound floods upon
686 combined rainfall and storm surge events in a low-lying coastal city. Journal of Hydrology,
687 627, 130476. doi: 10.1016/j.jhydrol.2023.130476
688 Genz, F. & Lessa, G. 2015. Twenty-six years of uneven changes in low flows due to different uses
689 and operation of a large dam in a semiarid river. Revista Brasileira De Recursos Hídricos,
690 20(2), 523–532. doi: 10.21168/rbrh.v20n2.p523-532.
691 Gramcianinov, C. B., De Camargo, R., Campos, R. M., Soares, C. G. & Da Silva Dias, P. L. 2022. Impact
692 of extratropical cyclone intensity and speed on the extreme wave trends in the Atlantic
693 Ocean. Climate Dynamics, 60(5–6), 1447–1466. doi: 10.1007/s00382-022-06390-2.
694 Gramcianinov, C. B., Staneva, J., De Camargo, R. & Da Silva Dias, P. L. 2023. Changes in extreme
695 wave events in the southwestern South Atlantic Ocean. Ocean Dynamics, 73(11), 663–678.
696 doi: 10.1007/s10236-023-01575-7.
697 Hamlington, B. D., Bellas-Manley, A., Willis, J. K., Fournier, S., Vinogradova, N., Nerem, R. S., Piecuch,
698 C. G., Thompson, P. R. & Kopp, R. 2024. The rate of global sea level rise doubled during the
699 past three decades. Communications Earth & Environment, 5(1). doi:
700 10.1038/s43247-024-01761-5.
701 Hamlington, B. D., Cheon, S. H., Piecuch, C. G., Karnauskas, K. B., Thompson, P. R., Kim, K., Reager, J.
702 T., Landerer, F. W. & Frederikse, T. 2019. The dominant global modes of recent internal sea
703 level variability. Journal of Geophysical Research Oceans, 124(4), 2750–2768. doi:
704 10.1029/2018jc014635.
705 Harrison, C. G. A. 2002. Power spectrum of sea level change over fifteen decades of frequency.
706 Geochemistry Geophysics Geosystems, 3(8), 1–17. doi: 10.1029/2002gc000300.
707 Hinton, A. C. 1995. Holocene tides of The Wash, U.K.: The influence of water-depth and
708 coastline-shape changes on the record of sea-level change. Marine Geology, 124(1–4),
709 87–111. doi: 10.1016/0025-3227(95)00034-v.
710 IBGE. (2022). Censo 2022 – Censo Cidades.
711 https://cidades.ibge.gov.br/brasil/ba/salvador/pesquisa/10101/96387.
712 Jevrejeva, S., Grinsted, A. & Moore, J. C. 2009. Anthropogenic forcing dominates sea level rise since

1850. Geophysical Research Letters, 36(20). doi: 10.1029/2009gl040216.

Lima, G. M. P. & Lessa, G. C. 2001. The fresh-water discharge in Todos os Santos Bay (BA) an its significance to the general water circulation. Pesquisas Em Geociências, 28(2), 85. doi: 10.22456/1807-9806.20271.

Llovel, W., Balem, K., Tajouri, S. & Hochet, A. 2023. Cause of substantial global mean sea level rise over 2014–2016. Geophysical Research Letters, 50(19). doi: 10.1029/2023gl104709.

Lyddon, C., Brown, J. M., Leonardi, N. & Plater, A. J. 2018. Uncertainty in estuarine extreme water level predictions due to surge-tide interaction. PLoS ONE, 13(10), e0206200. doi: 10.1371/journal.pone.0206200

Melo. 2017. Maré meteorológica na costa brasileira (Full Professor Thesis). Federal University of Rio Grande. Retrieved from https://sistemas.furg.br/sistemas/sab/arquivos/conteudo_digital/000008808.pdf.

Muis, S., Aerts, J. C. J. H., Antolínez, J. a. Á., Dullaart, J. C., Duong, T. M., Erikson, L., Haarsma, R. J., Apecechea, M. I., Mengel, M., Bars, D. L., O'Neill, A., Ranasinghe, R., Roberts, M. J., Verlaan, M., Ward, P. J. & Yan, K. 2023. Global projections of storm surges using High-Resolution CMIP6 climate models. Earth's Future, 11(9). doi: 10.1029/2023ef003479.

Nicolodi, J. L. & Petermann, R. M. 2010. Mudanças Climáticas e a Vulnerabilidade da Zona Costeira do Brasil: Aspectos ambientais, sociais e tecnológicos. Revista De Gestão Costeira Integrada, 10(2), 151–177. doi: 10.5894/rgci206.

Pawlowicz, R., Beardsley, B. & Lentz, S. 2002. Classical tidal harmonic analysis including error estimates in MATLAB using T_TIDE. Computers & Geosciences, 28(8), 929–937. doi:10.1016/s0098-3004(02)00013-4.

Peng, D., Hill, E. M., Meltzner, A. J. & Switzer, A. D. 2019. Tide Gauge Records Show That the 18.61-Year Nodal Tidal Cycle Can Change High Water Levels by up to 30 cm. Journal of Geophysical Research Oceans, 124(1), 736–749. doi: 10.1029/2018jc014695.

Pereira, J., Santos, J.V.B., Lessa, G.C. & Barreto, B.A. The wave climate and well events from ten-year in situ time series at the continental shelf of northern Bahia, Brazil. Ocean and Coastal Oceanography (submitted).

Pickering, M. D., Wells, N. C., Horsburgh, K. J. & Green, J. A. M. 2011. The impact of future sea-level rise on the European Shelf tides. Continental Shelf Research, 35, 1–15. doi: 10.1016/j.csr.2011.11.011.

Piecuch, C. G. & Ponte, R. M. 2015. Inverted barometer contributions to recent sea level changes along the northeast coast of North America. Geophysical Research Letters, 42(14), 5918–5925. doi: 10.1002/2015gl064580.

Ray, R. D. & Merrifield, M. A. 2019. The semiannual and 4.4-Year modulations of extreme high tides. Journal of Geophysical Research Oceans, 124(8), 5907–5922. doi:10.1029/2019jc015061

Santos, F. M., Lessa, G. C., Cirano, M., Domingues, R. M. & Lentini, C. A. D. 2015. Localized coastal upwelling at the Brazil Current formation zone (13°S). Proceedings of the XVII Simpósio Brasileiro de Sensoriamento Remoto. Available at: https://www.researchgate.net/publication/280925148_Localized_coastal_upwelling_at_the_Brazil_Current_formation_zone_13S

Schettini, C. A. F., Truccolo, E. C., Mattos, J. A. D. & Benevides, D. C. D. A. 2019. Tides and sea level

variability decomposition in the Port of Santos Waterway. Brazilian Journal of Oceanography, 67. doi: 10.1590/s1679-87592019026506707.

SEFAZ – Secretaria Municipal da Fazenda - Prefeitura Municipal de Salvador. 2017. Nuvem de pontos LiDAR, carta Salvador, SD-24-X. Available at: https://cartografia.salvador.ba.gov.br/dados-geoespaciais/baixar-dados-geoespaciais Accessed: April 04, 2026.

Shaw, J., Amos, C. L., Greenberg, D. A., O'Reilly, C. T., Parrott, D. R. & Patton, E. 2010. Catastrophic tidal expansion in the Bay of Fundy, Canada Earth Sciences Sector (ESS) Contribution 20090423. *Canadian Journal of Earth Sciences*, *47*(8), 1079–1091. doi: 10.1139/e10-046

Spicer, P., Huguenard, K., Ross, L. & Rickard, L. N. 2019. High-Frequency Tide-Surge-River interaction in estuaries: Causes and implications for coastal flooding. *Journal of Geophysical Research Oceans*, *124*(12), 9517–9530. doi: 10.1029/2019jc015466

Thévenin, Pereira, J. & Lessa, G. C. 2019. Shelf-break upwelling on a very narrow continental shelf adjacent to a western boundary current formation zone. *Journal of Marine Systems*, *194*, 52–65. doi: 10.1016/j.jmarsys.2019.02.008.

Truccolo, E. C., Franco, D. & Schettini, C. A. F. 2006. The low frequency sea level oscillations in the northern coast of Santa Catarina, Brazil. *Journal of Coastal Research*, SI 39, 547-552. Available at: https://www.researchgate.net/publication/272742146_The_low_Frequency_Sea_Level_Oscillations_in_the_Northern_Coast_of_Santa_Catarina_Brazil.

University of Hawaii Sea Level Center (UHSLC). Quality assessment of sea level data: Salvador-B Station. https://uhslc.soest.hawaii.edu/rqds/metadata_yaml/708Bmeta.yaml. Accessed: November 20, 2025.

Vianna, H. D., Calliari, L. J. & Vianna, S. D. 2020. Inundação e erosão na costa norte do Rio Grande do Sul - Brasil. Estudo de caso: a maré meteorological de outubro de 2016. *Revista Brasileira De Geomorfologia*, *21*(4). doi: 10.20502/rbg.v21i4.1749

Zheng, C.-W., Li, X.-H., Azorin-Molina, C., Li, C.-Y., Wang, Q., Xiao, Z.-N., Yang, S.-B., Chen, X. & Zhan, C. 2022. Global trends in oceanic wind speed, wind-sea, swell, and mixed wave heights. *Applied Energy*, *321*, 119327. doi: 10.1016/j.apenergy.2022.119327

This preprint was submitted under the following conditions:

- The authors declare that the necessary Terms of Free and Informed Consent of participants or patients in the research were obtained and are described in the manuscript, when applicable.
- The authors declare that the preparation of the manuscript followed the ethical norms of scientific communication.
- The authors declare that they are aware that they are solely responsible for the content of the preprint and that the deposit in SciELO Preprints does not mean any commitment on the part of SciELO, except its preservation and dissemination.
- The authors declare that the data, applications, and other content underlying the manuscript are referenced.
- The deposited manuscript is in PDF format.
- The authors declare that the research that originated the manuscript followed good ethical practices and that the necessary approvals from research ethics committees, when applicable, are described in the manuscript.
- The authors declare that once a manuscript is posted on the SciELO Preprints server, it can only be taken down on request to the SciELO Preprints server Editorial Secretariat, who will post a retraction notice in its place.
- The authors agree that the approved manuscript will be made available under a Creative Commons CC-BY license.
- The submitting author declares that the contributions of all authors and conflict of interest statement are included explicitly and in specific sections of the manuscript.
- The authors declare that the manuscript was not deposited and/or previously made available on another preprint server or published by a journal.
- If the manuscript is being reviewed or being prepared for publishing but not yet published by a journal, the authors declare that they have received authorization from the journal to make this deposit.
- The submitting author declares that all authors of the manuscript agree with the submission to SciELO Preprints.